

Fragile symmetry-protected half metallicity in two-dimensional van der Waals magnets: A case study of monolayer FeCl₂

Qiushi Yao ¹, Jiayu Li ¹, and Qihang Liu^{1,2,3,*}

¹Shenzhen Institute for Quantum Science and Engineering and Department of Physics, Southern University of Science and Technology, Shenzhen 518055, China

²Guangdong Provincial Key Laboratory of Computational Science and Material Design, Southern University of Science and Technology, Shenzhen 518055, China

³Shenzhen Key Laboratory of Advanced Quantum Functional Materials and Devices, Southern University of Science and Technology, Shenzhen 518055, China



(Received 27 April 2021; accepted 22 June 2021; published 6 July 2021)

Two-dimensional (2D) half-metallic materials are of great interest for their promising applications in spintronics. Although numerous 2D half metals have been proposed theoretically, rarely can they be synthesized experimentally. Here, exemplified by monolayer FeCl₂, we show three mechanisms in such quantum magnets that would cause the metal-insulator transition by using first-principles calculations. In particular, half metallicity, especially that protected by symmetry-induced degeneracies, predicted by the previous theoretical simulations could be destroyed by electron correlation, spin-orbit coupling, and further structural distortions to lower the total energy. Our work reveals the fragility of the symmetry-protected half metals upon various competing energy-lowering mechanisms, which should be taken into account for theoretically predicting and designing quantum materials with exotic functionalities.

DOI: [10.1103/PhysRevB.104.035108](https://doi.org/10.1103/PhysRevB.104.035108)

I. INTRODUCTION

Two-dimensional van der Waals (2D vdW) magnetic materials exfoliated from their bulk counterparts have gained extensive attention since the successful synthesis of atomically thin CrI₃ [1], Cr₂Ge₂Te₆ [2], and Fe₃GeTe₂ [3] flakes. These 2D vdW magnets with intrinsic magnetic properties provide an ideal platform for exploring the long-range magnetic order in the 2D limit, showing promising applications in next-generation spintronic devices. Practical applications of 2D vdW magnets require considerable magnetocrystalline anisotropy energy (MAE) and room-temperature T_C , which are the main focuses of most previous studies [3,4]. Yet, another typical character of these 2D vdW magnets is that most of them are 3d transition-metal compounds, which provides unique opportunities for studying the coupling between magnetism (Hund's interaction as well as Jahn-Teller effect) and electron correlation. Such phenomena have been widely studied in perovskites, leading to a plethora of exotic effects featured by charge, spin, and orbital degrees of freedom [5–7]. However, only rarely are such phenomena mentioned in the present literature devoted to 2D vdW magnets [8–10]. Furthermore, from 3d to 4d and 5d transition-metal 2D vdW magnets, albeit larger crystal-field splitting and weaker Hund's interaction entail them preferring low-spin states, which suppresses the magnetism, strong intrinsic spin-orbit coupling (SOC) brings about interesting and nontrivial effects and acts as another knob to tune the properties of 2D vdW

magnets, such as the well-known iridate Sr₂IrO₄ [11]. In addition to providing MAE that harbors 2D magnetism, how SOC will affect the properties of 2D vdW magnets is another interesting and fundamental problem.

Very recently, a new 2D vdW magnet, i.e., FeCl₂, has been synthesized by molecular-beam epitaxy [12,13]. With a nominal valent state of +2, each octahedrally coordinated Fe²⁺ ion holds six *d* electrons with the population of $t_{2g}^{3\uparrow} e_g^{2\uparrow}$ and $t_{2g}^{1\downarrow}$, possessing high-spin state [12,13]. Theoretical studies predicted monolayer FeCl₂ as a SOC-assisted Mott insulator with the spin-down electron occupying a nondegenerate orbital guaranteed by local trigonal distortion and SOC [14]. However, many other theoretical studies predicted a half-metallic state [12,15–19]. Indeed, Cai *et al.* demonstrated that FeCl₂ monolayer is a uniform insulator with a gap in the magnitude of an electronvolt [13]. However, it was mentioned in the study that the observed insulating nature of monolayer FeCl₂ may be an extrinsic property other than an intrinsic one. Extra charge transfer from graphite to FeCl₂ may shift the Fermi level and induce a gap in FeCl₂ [13]. Controversies between various studies call for prompt theoretical and experimental verifications.

In this work, exemplified by monolayer FeCl₂, we endeavor to obtain a microscopic insight into the discrepancy between theoretical and experimental studies. By employing density-functional theory (DFT) calculations, we show that the predicted “robust” half metallicity of monolayer FeCl₂ is actually guaranteed by the coexistence of orbital ordering (lower-lying e'_g and higher-lying a_{1g}) and symmetry-protected double degeneracy of e'_g . However, such half metallicity tends

*liuqh@sustech.edu.cn

to be destroyed by considering some realistic symmetry-breaking mechanisms, i.e., SOC and structural distortions. Furthermore, we find that electron correlation can switch the a_{1g} - e'_g relative order, leading to metal-insulator transition of monolayer FeCl_2 . Our work not only reveals the fragility of the exotic symmetry-protected half metals upon energy-lowering mechanisms, but also sheds light on the rational ground-state prediction by avoiding local minima in first-principles calculations.

II. COMPUTATIONAL METHODOLOGY

First-principles calculations were carried out using the Vienna *Ab initio* Simulation Package (VASP) [20] within the framework of DFT [21,22]. Exchange-correlation functional was described by generalized gradient approximation (GGA) with the Perdew-Burke-Ernzerhof formalism [23]. The electron-ion interaction was treated by projector augmented wave potentials [24] with a plane-wave basis cutoff of 500 eV. The whole Brillouin zone was sampled by $15 \times 15 \times 1$ Monkhorst-Pack grid [25] for monolayer FeCl_2 . Due to the correlation effects of $3d$ electrons in Fe atoms, we employed the GGA+ U approach within the Dudarev scheme [26]. A large scale of U (0.1–4 eV) was applied to study the evolution of electronic properties with U . We took the experimental lattice constant, namely, $a = b = 3.603 \text{ \AA}$ [27], and kept it unchanged through structural optimization. (For comparison, we also optimized the lattice constant, which converged to 3.592 \AA , in consistency with the experimental value. See Fig. S1 of the Supplemental Material [28] for the evolution of optimized lattice constants with U .) A vacuum space larger than 15 \AA was employed to avoid artificial periodic image interactions between FeCl_2 layers. All atoms were fully relaxed until the force on each atom was less than 0.01 eV/ \AA and the total energy minimization was performed with a tolerance of 10^{-5} eV. A $4 \times 4 \times 1$ supercell was constructed and relaxed without any symmetry constraints to investigate further structural distortions. The Brillouin zone of the supercell was sampled by $5 \times 5 \times 1$ Monkhorst-Pack grid. Open-source code BANDUP [29,30] was used to unfold the supercell band structure to get the effective band structure (EBS).

It was worth mentioning that in order to avoid converging to the local minima of the potential-energy surface, we took two initial electron populations as the starting point, namely, $e'_g a_{1g}^0 e_g^0$ and $e_g^0 a_{1g}^1 e'_g^0$, and then did self-consistent calculations including a full electronic relaxation (here we only considered possible occupation configurations of the single property-determining spin-down electron). Both populations can be achieved by assuming an initial electron occupation matrix via the open-source software developed by Watson [31] (see Supplemental Material [28], Computational Methodology for more details). By this procedure, we can reliably get the ground state by a direct comparison of the two different configurations. Such procedure was necessary to determine the ground state of monolayer FeCl_2 and has been widely used in previous studies [10,32–34]. For simplicity, we marked the state wherein the $d^{1\downarrow}$ electron occupies e'_g doublet as e'_g^1 instead of $e'_g a_{1g}^0 e_g^0$, and the state wherein the $d^{1\downarrow}$ electron occupies a_{1g} singlet as a_{1g}^1 to replace $e_g^0 a_{1g}^1 e_g^0$. Open-source

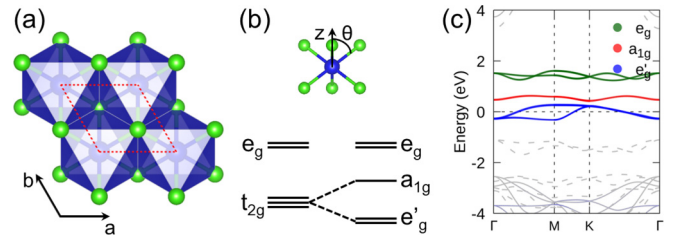


FIG. 1. (a) Crystal structure of monolayer FeCl_2 . Red dashed lines outline the unit cell. Blue and green spheres represent Fe and Cl atoms, respectively. The FeCl_6 octahedra are colored blue. (b) Compressed local trigonal distortion featured by $\theta > \theta_0$, where θ is the angle between the z axis (here is the crystallographic c axis) and Fe–Cl bonds. In undistorted octahedron, $\theta_0 = 54.74^\circ$. Crystal-field splitting diagram of d orbitals induced by octahedral crystal field and trigonal distortion. For simplicity, we show here a_{1g} singlet is higher than e'_g doublet, while the reversed order is also possible (see text for details). (c) Band structure calculated by spin-unrestricted GGA method with initial electron population $e'_g a_{1g}^0 e_g^0$, leading to the final e'_g^1 state. The spin-down Fe- $3d$ orbitals are highlighted in different colors. Spin-up and spin-down channels are indicated by dashed and solid lines, respectively.

software VESTA [35] and VASPKIT [36] were used to visualize and deal with VASP output files.

III. RESULTS AND DISCUSSION

A. Basic electronic structure

As shown in Fig. 1(a), monolayer FeCl_2 crystallizes in T -phase monolayer MoS_2 structure (space group $P-3m1$) with the Fe layer sandwiched between two Cl layers. Each Fe atom is surrounded by six first-neighbor Cl atoms forming an FeCl_6 octahedron, arranged in an edge-sharing pattern. In the absence of any distortion, the octahedral crystal field splits Fe- $3d$ orbitals into the lower-lying triply degenerate t_{2g} and the higher-lying doubly degenerate e_g orbitals. Taking the 2D nature of the monolayer and the local compressed trigonal distortion into account (featured by $\theta > \theta_0 = 54.74^\circ$) [10,14,37], the triply degenerated t_{2g} orbitals are split into a_{1g} singlet and e'_g doublet, as schematized in Fig. 1(b). As anticipated, the band structure calculated by the pure spin-restricted GGA calculations demonstrates the crystal-field levels, as illustrated in Fig. S2 [28]. The energy splitting between the entirely occupied t_{2g} and empty e_g manifolds is about 1.5 eV, while the local trigonal distortion-induced gap between a_{1g} and e'_g levels is about an order of magnitude smaller, a hallmark of second-order effect compared with the octahedral crystal-field splitting. Due to the similar energies between a_{1g} and e'_g manifolds, the a_{1g} - e'_g relative order is more subtle, which depends on the crystal shape (compressed or elongated trigonal distortion), electron filling, e'_g - e_g mixing, and long-ranged crystal field due to the lattice anisotropy [38,39]. The hierarchy of a_{1g} and e'_g levels is especially prominent for determining the ground state of monolayer FeCl_2 , which will be detailed below (Mechanism I).

Further considering the Hund's interaction, monolayer FeCl_2 possesses high-spin ground state with the electron population of $d^{5\uparrow}d^{1\downarrow}$, giving the total moment of $4 \mu_B/f.u.$

[see Fig. 1(c)], in consistency with the previous experimental measurements [27,40,41] and theoretical studies [12,14–18]. Our calculations show that both initial starting points, $e_g^1 a_{1g}^0 e_g^0$ and $e_g^0 a_{1g}^1 e_g^0$, converge to final e_g^1 configuration, as shown in Figs. 1(c) and S3 [28]. The spin-down e_g^1 doublet encompasses the Fermi level, while the a_{1g} singlet resides between e_g^1 and e_g states. In fact, at Γ (K), the two e_g^1 orbitals form the basis function $\{\frac{1}{\sqrt{3}}(d_{xy} + e^{i2\pi/3}d_{xz} + e^{i4\pi/3}d_{yz}), \frac{1}{\sqrt{3}}(d_{xy} + e^{i4\pi/3}d_{xz} + e^{i2\pi/3}d_{yz})\}$ (local coordinate) of a twofold irreducible representation of the little group D_{3d} (D_3), leading to symmetry-enforced double degeneracy. When only one electron occupies the doubly degenerated e_g^1 orbitals, monolayer FeCl_2 exhibits intrinsic half metallicity, consistent with the previous studies [12,15–19]. Such symmetry-protected half metallicity is robust as long as the specific orbital ordering (lower-lying e_g^1 and higher-lying a_{1g}) and symmetry (double degeneracy) coexist. However, as will be detailed below, the desired coexistence could be easily destroyed by electron correlation (Mechanism I), spin-orbit coupling (Mechanism II), and further symmetry-breaking energy-lowering distortions (Mechanism III). All these mechanisms tend to lift the coexistence, resulting in metal-insulator transition of FeCl_2 .

1. Mechanism I: Electron correlation-induced orbital switching

Firstly, we carry out spin-unrestricted GGA+ U calculations to elucidate the electron correlation effect at a mean-field level. As we will see, moderate correlation can switch the a_{1g} - e_g^1 ordering, leading to metal-insulator transition of FeCl_2 . A wide range of U (0.1–4 eV) is tested to ascertain the band evolution with U . On one hand, as can be seen from Fig. 2(a) (also see Fig. S4 [28]), starting from e_g^1 occupation as the initial configuration for electron density, the band structures calculated with all U results in half-metallic ground state. In fact, without any symmetry broken, any reasonable U or other functional (such as meta-GGA and hybrid functional; see Fig. S6(a) [28]) cannot break the double degeneracy at Γ and K . The increase of U only pushes the a_{1g} orbital far away from Fermi level but cannot split the e_g^1 doublet at these high-symmetry momenta, leading to the seemingly “robust” half-metallic phase reported in the literature [12,15–19]. On the other hand, starting from a_{1g}^1 , we get totally different results. Except for $U = 0.1$ eV, from $U = 0.2$ to 4 eV, all $e_g^0 a_{1g}^1 e_g^0$ starting point can converge to a_{1g}^1 , as shown in Figs. 2(b) and S5 [28]. Even with U as small as 0.2 eV (Fig. S5(b) [28]), the a_{1g}^1 electron population can induce a gap between a_{1g} and e_g^1 orbitals, leading to an insulator phase. Increasing U from 0.2 to 4 eV (Figs. 2(b) and S5 [28]), monolayer FeCl_2 maintains insulation with monotonically enhanced gap size because e_g^1 orbitals are pushed away from the Fermi level by U . Unlike the partially occupied e_g^1 orbitals in e_g^1 , bandwidth of the totally unoccupied e_g^1 orbitals in a_{1g}^1 configuration is suppressed by U evidently. At $U = 0.1$ eV (Fig. S5(a) [28]), initial a_{1g}^1 distribution converges to e_g^1 as the ground state (same as the case without U ; see Fig. S3 [28]). Potential surface at $U \leq 0.1$ eV is illustrated in the left panel of Fig. 2(e); a_{1g}^1 turns out to be an unstable configuration.

To determine the ground state between the two local minima for $U = 0.2$ to 4 eV, we compare the total energies of

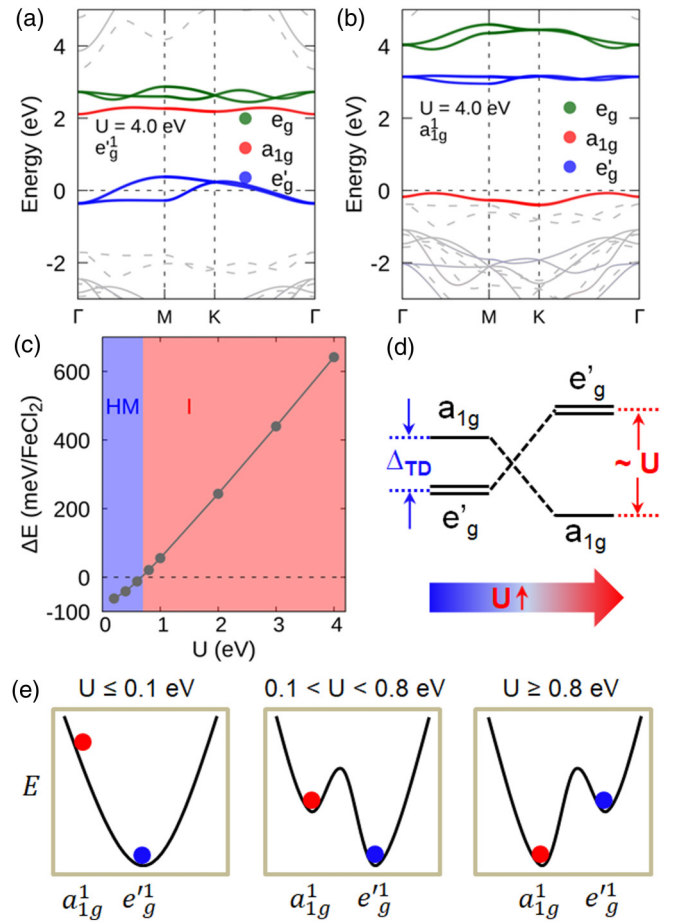


FIG. 2. (a) Band structure calculated by spin-unrestricted GGA+ U (4 eV) method. The initial electron population is $e_g^1 a_{1g}^0 e_g^0$, leading to the final e_g^1 state. (b) Same as (a) but starts from initial electron population $e_g^0 a_{1g}^1 e_g^0$, leading to the final a_{1g}^1 state. (c) Energy difference between e_g^1 and a_{1g}^1 states as a function of U , $\Delta E = E(e_g^1) - E(a_{1g}^1)$. HM stands for half metal. I stands for insulator. (d) Schematic plot shows the competing effect between trigonal distortion Δ_{TD} and on-site Hubbard U . Orbital ordering can be reversed by sufficient U . (e) Schematic plot showing the potential surfaces at different U .

these two states. As illustrated in Fig. 2(c), with U smaller than 0.8 eV, half-metallic e_g^1 state is favored in energy, while insulating a_{1g}^1 state becomes more energetically favorable with larger U (0.8–4 eV). For Fe, the reasonable U would be in the range of 2–4 eV [42,43]. The ground state is further confirmed by hybrid functional [44,45] calculations, obtaining that a_{1g}^1 state is more stable than e_g^1 state by 705 meV/ FeCl_2 (see Fig. S6 [28]). Thus, based on our calculations, it is reasonable to suggest that with moderate electron correlation, FeCl_2 favors the insulating ground state, which is confirmed by a recent experiment [13]. To obtain the insulating a_{1g}^1 state, moderate electron correlation and proper initial electron occupation matrix should be taken into account. As illustrated in the middle (right) panel of Fig. 2(e), a_{1g}^1 (e_g^1) configuration plays as a local minimum of the potential surface while e_g^1 (a_{1g}^1) configuration is ground state at $0.1 < U < 0.8$ eV ($U \geq 0.8$ eV). Another intriguing difference between a_{1g}^1 and

e'_g is that while a_{1g}^1 is a spin-only configuration ($l_z = 0$), e'_g renders monolayer FeCl_2 a state with orbital degree of freedom, resulting in fruitful orbital physics under certain conditions, especially after considering spin-orbit coupling (Mechanism II).

Based on the above analysis, we see that crystal field (including Jahn-Teller effect, i.e., local trigonal distortion here) and electron correlation act as competing effects in determining the ground state of monolayer FeCl_2 . Orbital ordering of a_{1g} - e'_g can be switched by electron correlation. As schematized in Fig. 2(d), without U (or small U), local trigonal distortion splits t_{2g} triplet into higher-lying a_{1g} singlet and lower-lying e'_g doublet. The a_{1g} - e'_g gap is determined by the trigonal distortion Δ_{TD} , which is typically tens to hundreds of meV. Further considering the electron correlation featured by the on-site Hubbard U , Coulomb repulsion raises the energy of partially filled e'_g orbitals. Sufficient U (here ~ 0.8 eV) will reverse the orbital ordering, resulting in metal-insulator transition. Typical U in $3d$ transition compounds is about several eV (comparable to the magnitude of octahedral crystal field), much larger than Δ_{TD} . Thus, the final gap is almost determined by the on-site Hubbard U . From $3d$ to $4d$ and $5d$ transition compounds, although the electron correlation is reduced, the typical on-site Hubbard U is still of the magnitude of eV. We expect that the aforementioned conclusion still holds.

2. Mechanism II: Degeneracy lifted by SOC

Spin-orbit coupling is another important ingredient in the determination of electronic properties, which may induce a plethora of nontrivial effects such as topological phase transition. We next perform GGA + U + SOC calculations to study the SOC effect. Same as the previous procedures, we start from two configurations of occupation, namely, e'_g and a_{1g}^1 . Owing to the unquenched orbital momentum, e'_g orbitals are SOC-active states, which can form complex orbitals with $l_z = \pm 1$, breaking the double degeneracy of e'_g . In this case, SOC entails the half-metallic e'_g state into an insulating state [14]. In the spin-down channel, SOC lowers $l_z = 1$ (labeled as e'_{g+}) state, and the $l_z = -1$ (labeled as e'_{g-}) state is pushed away from the Fermi level, leading to the final $e'_{g+} e'_{g-} a_{1g}^0 a_{1g}^0$ population (labeled as e'_{g+}). Figure 3(a) shows this mechanism exactly [compare with Fig. 2(a)]. It is worthwhile noticing that (at least most of) the large splitting between e'_{g+} and e'_{g-} is not solely contributed by SOC but also by electron correlation ($U = 4$ eV). Actually, at small U (0.1–0.4 eV), the e'_{g+} - e'_{g-} splitting is negligible. Band structures calculated with these U still exhibit half-metallic characteristics (see Figs. S7(a) to S7(c) [28]). However, from $U = 0.8$ to 4 eV, cooperative effects of SOC and electron correlation gaps e'_{g+} and e'_{g-} states make monolayer FeCl_2 a spin-orbit assisted Mott insulator, just like the famous iridate Sr_2IrO_4 [11]. Although in light elements, such as Fe and Cl, intrinsic SOC is much lower than that in $5d$ transition-metal iridium, the much stronger electron correlation becomes substantial for gap opening. Subtle balance between SOC and Hubbard correlation entails monolayer FeCl_2 preferring insulating other than half-metallic state.

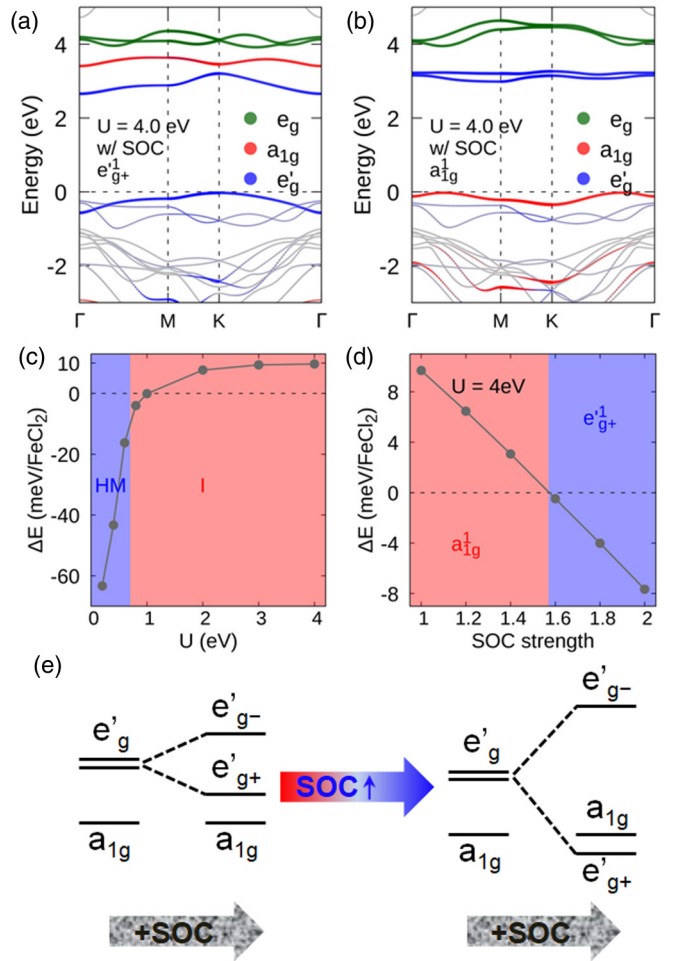


FIG. 3. (a) Band structure calculated by GGA+ U (4 eV)+SOC method. The initial electron population is e'_g , leading to the final e'_{g+} state. (b) Same as (a) but starts from initial electron population a_{1g}^1 , leading to the final a_{1g}^1 state. (c) Energy difference between e'_{g+} and a_{1g}^1 states as a function of U , $\Delta E = E(e'_{g+}) - E(a_{1g}^1)$. HM stands for half-metal. I stands for insulator. (d) Energy difference between e'_{g+} and a_{1g}^1 states as a function of SOC strength. (e) Schematic plot shows the orbital ordering can be reversed by sufficient magnitude of SOC.

At variance with e'_g , Fig. 3(b) shows the band structure calculated starting from a_{1g}^1 (also see Fig. S8 [28]). As aforementioned, a_{1g}^1 is a spin-only state, further considering the SOC effect does not bring about significant band modification. Tiny splitting can be observed in the first and second conduction bands (e'_{g+} - e'_{g-} splitting). Since both e'_{g+} and e'_{g-} levels are unoccupied, the splitting between the two levels is dictated by SOC effects. Again, to ascertain the ground state of monolayer FeCl_2 , it is necessary to compare the energy of e'_{g+} and a_{1g}^1 . As illustrated in Fig. 3(c), monolayer FeCl_2 prefers e'_{g+} with U smaller than 1 eV, while for larger U it favors a_{1g}^1 . The half-metal–insulator transition occurs at $U \sim 0.7$ eV. Energy difference between e'_{g+} and a_{1g}^1 converges progressively with the increase of U , which can be ascribed to the similar insulating band structures, regardless of different orbital ordering, in sharp contrast to e'_g and a_{1g}^1 [Fig. 2(c)].

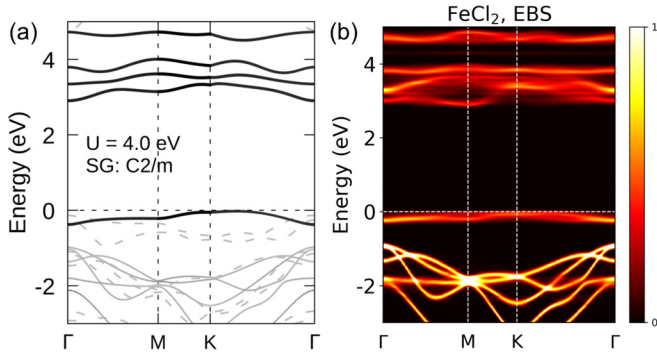


FIG. 4. (a) Band structure of FeCl_2 with space group $C2/m$ calculated by $GGA+U$ (4 eV) method. The spin-down $\text{Fe-}3d$ orbitals are highlighted by black. Spin-up and spin-down channels are indicated by dashed and solid lines, respectively. (b) Effective band structure of FeCl_2 $4 \times 4 \times 1$ supercell with space group $P1$. The color scale represents the spectral weight of the k character for the primitive Brillouin zone. For clarity, we only show the spin-down channel here.

Meanwhile, the strength of SOC can serve as another knob to tune the orbital ordering of monolayer FeCl_2 . Figure 3(d) shows that at $U = 4$ eV, a_{1g}^1 can transit to e_{g+}^1 when the magnitude of SOC is as strong as 1.6 times of the original strength. In particular, SOC lowers the e_{g+}^1 state of FeCl_2 but hardly affects the a_{1g} state; gradually enhanced SOC strength modifies $a_{1g}-e_{g+}^1$ ordering, as schematized in Fig. 3(e). Due to weaker electron correlation and stronger SOC, this phenomenon is ready to occur in $5d$ transition-metal compounds, such as in $\text{Sr}_3\text{NiIrO}_6$, orbital ordering induced by crystal field eventually reversed by strong SOC of iridium [33].

3. Mechanism III: Further symmetry-breaking energy-lowering distortions

At last, we discuss the lift of degeneracy by the further structural distortions. Notice that in e_g^1 without SOC, spin-down e_g^1 doublet encompasses the Fermi level, which tends to result in symmetry-breaking Jahn-Teller distortions to lower the total energy. Such effect has been widely studied in transition-metal perovskite oxides, dubbed as one important gap-opening mechanism [34]. Possible symmetry-breaking distortions include octahedra tilting, rotation, breathing, and so on. So, we carry out $DFT + U$ (4 eV) calculations starting from e_g^1 and relax the structure without any enforced symmetry constraints (lattice constant is fixed to experimental value 3.603 Å; see Sec. II for details). As anticipated, the relaxed structure lowers its symmetry with the final space group $C2/m$. Compared with $P-3m1$ FeCl_2 [Fig. 1(a)], after relaxation, two inequivalent Cl atoms of $C2/m$ FeCl_2 move in opposite directions, breaking the threefold rotational symmetry (see Fig. S9 [28]). Meanwhile, symmetry lowering lifts the degeneracy of e_g^1 and e_g orbitals, leading to metal-insulator transition [Fig. 4(a)]. Such state is 675 meV lower than e_g^1 and 33 meV lower than a_{1g}^1 , respectively. Furthermore, we construct a $4 \times 4 \times 1$ supercell to relax the structure with more degree of freedom. Without any symmetry constraints, the relaxed structure possesses space group $P1$. Figure 4(b) shows the EBS of FeCl_2 supercell. Apart from the band broadening

induced by structural disorder, we can see five nondegenerate d -orbital states between -0.5 and 5 eV obviously. Thus, apart from the orbital ordering mechanism, half metallicity of FeCl_2 may also be excluded by possible structural distortions. In other words, “symmetry-guaranteed” half metal is somehow fragile when the half metallicity is created by the partial filling of symmetry-enforced degeneracy states. Various symmetry-breaking energy-lowering distortions tend to lift the degeneracy, resulting in metal-insulator transition.

IV. DISCUSSION AND CONCLUSION

Finally, we would like to briefly discuss the possible charge-transfer mechanism that may lead “half-metallic” (e_g^1) FeCl_2 to be an insulator [13]. To investigate the effect of charge transfer, we carried out band-structure calculations of FeCl_2 monolayer with various doping concentrations (from 0 to $1e/\text{FeCl}_2$) by using virtual crystal approximation [46,47] at $DFT+U$ (4 eV) level. As shown in Fig. S10 [28], starting from metallic FeCl_2 (e_g^1 , Fig. S10(a) [28]), electron injection moves Fermi level upward gradually without leading considerable modification to the band structure, keeping FeCl_2 metallic until a high doping concentration $0.8e/\text{FeCl}_2$ (Figs. S10(b) to S10(e) [28]). Reaching $1e/\text{FeCl}_2$ doping concentration, FeCl_2 undergoes metal-insulator transition with fully occupied e_g^1 states (see Fig. S10(f) [28]). Such a strong and precise doping concentration is unlikely to occur through the substrates of FeCl_2 such as graphite [13]. Therefore, in our opinion, the insulating nature of FeCl_2 monolayer is more likely to be an intrinsic property other than an extrinsic one induced by extra electron injection from substrates.

In summary, exemplified by monolayer FeCl_2 , our calculations demonstrate three mechanisms leading half-metallic FeCl_2 to be an insulator. Firstly, electron correlation reverses crystal-field levels, rendering FeCl_2 a Mott insulator with the spin-down electron occupying a_{1g} singlet. Band gap between a_{1g} and e_g^1 can be ascribed to the magnitude of Hubbard correlation. Secondly, starting from e_g^1 , SOC splits the partially occupied e_g^1 doublet, making FeCl_2 a SOC-assisted Mott insulator. Starting from a_{1g} , SOC splits the unoccupied e_g^1 doublet without leading to considerable modification to the band structure. Correlation and SOC act cooperatively to suppress the half metallicity of monolayer FeCl_2 . Gradually enhanced SOC will reverse $a_{1g}-e_{g+}^1$ ordering but maintains the insulation, which may occur in $4d$ and $5d$ 2D materials. Thirdly, further symmetry-breaking structural distortions tend to lift the double degeneracy of e_g^1 , leading to the metal-insulator transition of FeCl_2 . Our results indicate that similar to 3D transition-metal compounds, charge, spin, and orbital degrees of freedom can induce fruitful exotic effects in 2D magnets and should be treated properly. Nowadays, high-throughput simulation accelerates the process of material design. However, for complex quantum materials, which are hard to handle by naive DFT calculations, extra filters should be added to avoid plausible predictions of fantasy materials.

ACKNOWLEDGMENTS

This work was supported by National Key R&D Program of China (Grant No. 2020YFA0308900), the National Natural

Science Foundation of China (Grant No. 12004163), Post-doctoral Fellowship of Shenzhen (Grant No. K21207505), Guangdong Provincial Key Laboratory for Computational Science and Material Design (Grant No. 2019B030301001),

the Shenzhen Science and Technology Program (Grant No. KQTD20190929173815000), and Center for Computational Science and Engineering of Southern University of Science and Technology.

-
- [1] B. Huang, G. Clark, E. Navarro-Moratalla, D. R. Klein, R. Cheng, K. L. Seyler, D. Zhong, E. Schmidgall, M. A. McGuire, D. H. Cobden, W. Yao, D. Xiao, P. Jarillo-Herrero, and X. Xu, *Nature (London)* **546**, 270 (2017).
- [2] C. Gong, L. Li, Z. Li, H. Ji, A. Stern, Y. Xia, T. Cao, W. Bao, C. Wang, Y. Wang, Z. Q. Qiu, R. J. Cava, S. G. Louie, J. Xia, and X. Zhang, *Nature (London)* **546**, 265 (2017).
- [3] Y. Deng, Y. Yu, Y. Song, J. Zhang, N. Z. Wang, Z. Sun, Y. Yi, Y. Z. Wu, S. Wu, J. Zhu, J. Wang, X. H. Chen, and Y. Zhang, *Nature (London)* **563**, 94 (2018).
- [4] Z.-X. Shen, X. Bo, K. Cao, X. Wan, and L. He, *Phys. Rev. B* **103**, 085102 (2021).
- [5] Y. Tokura and N. Nagaosa, *Science* **288**, 462 (2000).
- [6] E. Dagotto, T. Hotta, and A. Moreo, *Phys. Rep.* **344**, 1 (2001).
- [7] E. Dagotto, *Science* **309**, 257 (2005).
- [8] C. Huang, F. Wu, S. Yu, P. Jena, and E. Kan, *Phys. Chem. Chem. Phys.* **22**, 512 (2020).
- [9] Y.-P. Wang and M.-Q. Long, *Phys. Rev. B* **101**, 024411 (2020).
- [10] K. Yang, F. Fan, H. Wang, D. I. Khomskii, and H. Wu, *Phys. Rev. B* **101**, 100402(R) (2020).
- [11] B. J. Kim, H. Jin, S. J. Moon, J. Y. Kim, B. G. Park, C. S. Leem, J. Yu, T. W. Noh, C. Kim, S. J. Oh, J. H. Park, V. Durairaj, G. Cao, and E. Rotenberg, *Phys. Rev. Lett.* **101**, 076402 (2008).
- [12] X. Zhou, B. Brzostowski, A. Durajski, M. Liu, J. Xiang, T. Jiang, Z. Wang, S. Chen, P. Li, Z. Zhong, A. Drzewiński, M. Jarosik, R. Szcześniak, T. Lai, D. Guo, and D. Zhong, *J. Phys. Chem. C* **124**, 9416 (2020).
- [13] S. Cai, F. Yang, and C. Gao, *Nanoscale* **12**, 16041 (2020).
- [14] A. S. Botana and M. R. Norman, *Phys. Rev. Mater.* **3**, 044001 (2019).
- [15] E. Torun, H. Sahin, S. K. Singh, and F. M. Peeters, *Appl. Phys. Lett.* **106**, 192404 (2015).
- [16] M. Ashton, D. Gluhovic, S. B. Sinnott, J. Guo, D. A. Stewart, and R. G. Hennig, *Nano Lett.* **17**, 5251 (2017).
- [17] Y. Feng, X. Wu, J. Han, and G. Gao, *J. Mater. Chem. C* **6**, 4087 (2018).
- [18] E. Ceyhan, M. Yagmurcukardes, F. M. Peeters, and H. Sahin, *Phys. Rev. B* **103**, 014106 (2021).
- [19] R. K. Ghosh, A. Jose, and G. Kumari, *Phys. Rev. B* **103**, 054409 (2021).
- [20] G. Kresse and J. Furthmüller, *Phys. Rev. B* **54**, 11169 (1996).
- [21] P. Hohenberg and W. Kohn, *Phys. Rev.* **136**, B864 (1964).
- [22] W. Kohn and L. J. Sham, *Phys. Rev.* **140**, A1133 (1965).
- [23] J. P. Perdew, K. Burke, and M. Ernzerhof, *Phys. Rev. Lett.* **77**, 3865 (1996).
- [24] G. Kresse and D. Joubert, *Phys. Rev. B* **59**, 1758 (1999).
- [25] H. J. Monkhorst and J. D. Pack, *Phys. Rev. B* **13**, 5188 (1976).
- [26] S. L. Dudarev, G. A. Botton, S. Y. Savrasov, C. J. Humphreys, and A. P. Sutton, *Phys. Rev. B* **57**, 1505 (1998).
- [27] M. K. Wilkinson, J. W. Cable, E. O. Wollan, and W. C. Koehler, *Phys. Rev.* **113**, 497 (1959).
- [28] See Supplemental Material at <http://link.aps.org/supplemental/10.1103/PhysRevB.104.035108> for the details of computational methodology, evolution of optimized lattice constants against U , band structures calculated by different methods, structural comparison between $P-3m1$ and $C2/m$ FeCl_2 , and band structures of electron-doped FeCl_2 .
- [29] P. V. C. Medeiros, S. Stafström, and J. Björk, *Phys. Rev. B* **89**, 041407(R) (2014).
- [30] P. V. C. Medeiros, S. S. Tsirkin, S. Stafström, and J. Björk, *Phys. Rev. B* **91**, 041116(R) (2015).
- [31] J. P. Allen and G. W. Watson, *Phys. Chem. Chem. Phys.* **16**, 21016 (2014).
- [32] B. Dorado, B. Amadon, M. Freyss, and M. Bertolus, *Phys. Rev. B* **79**, 235125 (2009).
- [33] X. Ou and H. Wu, *Sci. Rep.* **4**, 4609 (2014).
- [34] J. Varignon, M. Bibes, and A. Zunger, *Nat. Commun.* **10**, 1658 (2019).
- [35] K. Momma and F. Izumi, *J. Appl. Cryst.* **44**, 1272 (2011).
- [36] V. Wang, N. Xu, J.-C. Liu, G. Tang, and W.-T. Geng, *Comput. Phys. Commun.* **267**, 108033 (2021).
- [37] L. Hu, C. Xie, S. J. Zhu, M. Zhu, R. H. Wei, X. W. Tang, W. J. Lu, W. H. Song, J. M. Dai, R. R. Zhang, C. J. Zhang, X. B. Zhu, and Y. P. Sun, *Phys. Rev. B* **103**, 085119 (2021).
- [38] S. Landron and M.-B. Lepetit, *Phys. Rev. B* **77**, 125106 (2008).
- [39] H. Wu, C. F. Chang, O. Schumann, Z. Hu, J. C. Cezar, T. Burnus, N. Hollmann, N. B. Brookes, A. Tanaka, M. Braden, L. H. Tjeng, and D. I. Khomskii, *Phys. Rev. B* **84**, 155126 (2011).
- [40] I. S. Jacobs and P. E. Lawrence, *Phys. Rev.* **164**, 866 (1967).
- [41] R. J. Birgeneau, W. B. Yelon, E. Cohen, and J. Makovsky, *Phys. Rev. B* **5**, 2607 (1972).
- [42] F. Aryasetiawan, K. Karlsson, O. Jepsen, and U. Schönberger, *Phys. Rev. B* **74**, 125106 (2006).
- [43] Y. Yekta, H. Hadipour, E. Şaşıoğlu, C. Friedrich, S. A. Jafari, S. Blügel, and I. Mertig, *Phys. Rev. Mater.* **5**, 034001 (2021).
- [44] J. Heyd, G. E. Scuseria, and M. Ernzerhof, *J. Chem. Phys.* **118**, 8207 (2003).
- [45] F. Fuchs, J. Furthmüller, F. Bechstedt, M. Shishkin, and G. Kresse, *Phys. Rev. B* **76**, 115109 (2007).
- [46] L. Nordheim, *Ann. Phys.* **401**, 607 (1931).
- [47] L. Bellaiche and D. Vanderbilt, *Phys. Rev. B* **61**, 7877 (2000).